

Signatures of a Charge Ice State in the Doped Mott Insulator Nb_3Cl_8

Evgeny A. Stepanov*

*CPHT, CNRS, École polytechnique, Institut Polytechnique de Paris, 91120 Palaiseau, France and
Collège de France, Université PSL, 11 place Marcelin Berthelot, 75005 Paris, France*

The interplay between strong electronic correlations and the inherent frustration of certain lattice geometries is a common mechanism for the formation of nontrivial states of matter. In this work, we theoretically explore the collective electronic effects in the monolayer Nb_3Cl_8 , a recently discovered triangular lattice Mott insulator. Our advanced many-body numerical simulations predict the emergence of a phase separation region upon doping this material. Notably, in close proximity to the phase separation, the static charge susceptibility undergoes a drastic change and reveals a distinctive bow-tie structure in momentum space. The appearance of such a signature in the context of spin degrees of freedom would indicate the formation of a spin ice state. This finding allows us to associate the observed phase separation to a charge ice state, a state with a remarkable power-law dependence of both the effective exchange interaction and correlations between electronic densities in real space.

Mott insulators are among the most prominent examples of materials where the insulating behaviour does not arise from the band gap in the non-interacting electronic spectral function. Instead, it occurs as a result of strong local Coulomb repulsion that localizes the electrons on a lattice¹. These localized electrons typically form well-developed magnetic moments, leading to spatial magnetic fluctuations and the potential for a spin-ordered ground state at low temperatures. In this regard, Mott insulators are particularly promising for realizing exotic states such as the valence-bond, spin glass, or (quantum) spin liquid states². Doping Mott insulators usually suppresses magnetic fluctuations, but on the other hand, it may give rise to nontrivial collective electronic instabilities in the charge channel. For instance, it has been shown that doped Mott insulators can exhibit a first-order phase transition between either the Mott insulating or strongly correlated metallic phase and the weakly correlated metallic phase^{3–12}. This transition is associated with the appearance of a phase separation (PS) region, which is signaled by the divergence of the electronic compressibility or the charge susceptibility at zero momentum. Supplementing strong electronic correlation with the frustration that originates from a specific lattice geometry may result in the formation of more exotic phases. Thus, Mott insulators on a triangular lattice can reveal signatures of the chiral spin, charge, or superconducting states^{13–15}.

Finding an experimental realization of a Mott insulator is challenging. It requires identifying a system with a half-filled narrow band, which, without considering electronic interactions, is located at the Fermi energy and is distinctly decoupled from other bands. Furthermore, the Hubbard bands emerging from this narrow band upon including the interaction should also not hybridize with the rest of the energy spectrum. In this context, the recently discovered Mott insulator Nb_3Cl_8 , with an effective triangular geometry arising from the distorted kagome lattice, appears to be a promising candidate for realizing nontrivial states of matter. According to *ab-initio* theoretical calculations, this material exhibits a narrow half-filled band at the Fermi level^{16–19} and a very strong local interaction, which is approximately one order of magnitude larger than the bandwidth of the non-interacting electronic dispersion¹⁸. Such a strong Coulomb repulsion leads to a single-electron occupation of each lattice site, which makes the material a Mott insulator with a rather large gap. It has

been observed that at high temperatures, both the monolayer and bulk phases of Nb_3Cl_8 are paramagnetic, as confirmed by the Curie-Weiss behaviour of the spin susceptibility^{17,20}. At low temperatures, the bulk system undergoes a structural transition, leading to a nonmagnetic singlet ground state^{21,22}. In turn, the monolayer Nb_3Cl_8 is expected to form a 120° antiferromagnetic (AFM) ground state, as theoretically predicted based on Heisenberg model calculations.¹⁸

The characteristics of doped Nb_3Cl_8 have not been extensively addressed yet, with current research primarily focusing on its magnetic properties²⁰ and conductivity²³. The recent exciting results of Refs. 12–14, obtained for other triangular lattice Mott insulators, strongly encourage us to investigate collective electronic instabilities related to the charge fluctuations that may arise in Nb_3Cl_8 upon doping. To study many-body effects in the monolayer Nb_3Cl_8 , we use a single molecular orbital extended Hubbard model on an effective triangular lattice that was introduced in Ref. 18 based on *ab-initio* calculations. The corresponding model Hamiltonian

$$H = \sum_{j,j',\sigma} t_{jj'} c_{j\sigma}^\dagger c_{j'\sigma} - \mu \sum_j n_j + \frac{1}{2} \sum_{j,j'} U_{jj'} n_j n_{j'} \quad (1)$$

describes the hopping of electrons between the lattice sites j and j' with the hopping amplitude $t_{jj'}$ by means of the operators $c_{j\sigma}^{(\dagger)}$ that annihilate (create) an electron on the site j with the spin projection $\sigma \in \{\uparrow, \downarrow\}$. The chemical potential μ is included to the model to control the occupation of the orbital. In Nb_3Cl_8 , the Coulomb repulsion $U_{jj'}$ between the electronic densities $n_j = \sum_{\sigma} c_{j\sigma}^\dagger c_{j\sigma}$ is found to be extremely large compared to the non-interacting bandwidth and rather long-ranged¹⁸: The local interaction is equal to $U_{jj} \simeq 1.9$ eV and the interaction between the neighboring lattice sites $U_{\langle jj' \rangle}$ is only approximately 2.5 times smaller than the local one.

Accurately describing and predicting many-body effects, such as the formation of the Mott insulating state, magnetic fluctuations, and other manifestations of collective electronic behaviour, requires the use of advanced computational techniques. For this purpose, we employ the dual triply irreducible local expansion (D-TRILEX) method^{24–26}. This approach consistently accounts for a combined effect of local correlations, which are treated non-perturbatively via dynamical mean-field theory (DMFT)²⁷, and non-local collective

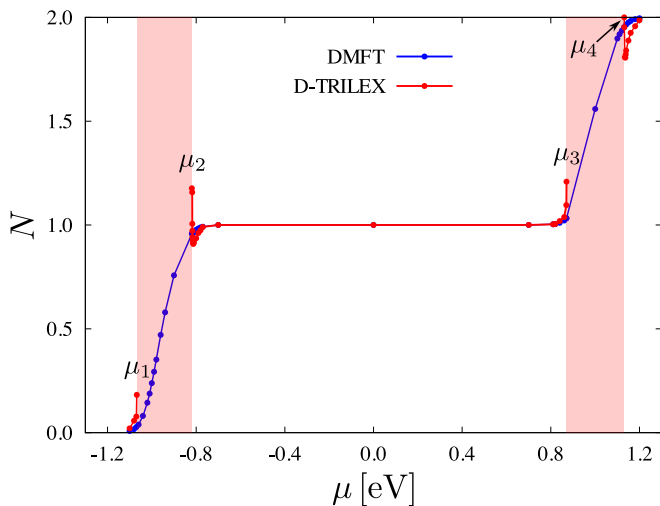


FIG. 1. Phase diagram. Dependence of the average electronic density N on the value of the chemical potential μ , where $\mu = 0$ corresponds to the case of an undoped monolayer Nb_3Cl_8 , calculated using the DMFT (blue) and D-TRILEX (red) methods. The chemical potentials μ_i correspond to the boundaries of the PS regions (shaded red areas). The result is obtained at $T = 290$ K.

electronic fluctuations, which are considered diagrammatically beyond DMFT^{28,29} without limitation on their range. D-TRILEX has been rigorously benchmarked against significantly more complex diagrammatic approaches, including exact solutions (when available)^{25,26}. It has been demonstrated that the method provides accurate results for the single-particle (electronic Green's function) and two-particle (charge and spin susceptibilities) response functions across a broad range of model parameters. The applicability of D-TRILEX spans from model calculations^{30–35} to realistic materials computations^{14,36,37}. The method is particularly useful for detecting various ordered phases that are determined by the divergence of the corresponding susceptibilities at the momentum that defines the wave vector of the ordering. Details on the D-TRILEX calculations for the considered model (1) are provided in the Methods section.

We begin investigating many-body effects in the monolayer Nb_3Cl_8 with the half-filled case. We perform calculations at two different temperatures, $T = 290$ K and 145 K. At both temperatures, in agreement with the results of previous works^{16–19}, we confirm that the material lies very deep in the Mott insulating phase: The obtained electronic spectral function features two narrow and nearly dispersiveless Hubbard bands separated by a large gap of the order of U_{jj} . However, we do not observe any signature of notable magnetic or charge fluctuations. The strength of the fluctuations can be estimated by looking at the largest static ($\omega = 0$) dielectric function $\epsilon_{\omega}^{\text{ch/sp}}(\mathbf{q}) = 1 + U^{\text{ch/sp}}(\mathbf{q})\Pi_{\omega}^{\text{ch/sp}}(\mathbf{q})$ in the corresponding (charge or spin) channel. The dielectric function is related to the susceptibility as $X_{\omega}^{\text{ch/sp}}(\mathbf{q}) = \Pi_{\omega}^{\text{ch/sp}}(\mathbf{q})/\epsilon_{\omega}^{\text{ch/sp}}(\mathbf{q})$ and shows how the polarization operator $\Pi_{\omega}^{\text{ch/sp}}(\mathbf{q})$ (irreducible with respect to the interaction $U^{\text{ch/sp}}(\mathbf{q})$ part of the susceptibility) is renormalized by the collective electronic fluctuations in

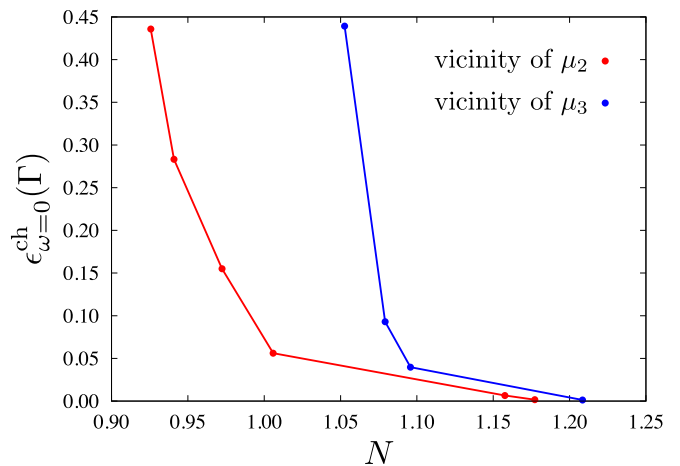


FIG. 2. Charge dielectric function in the vicinity of the PS. Evolution of the largest static dielectric function in the charge channel $\epsilon_{\omega=0}^{\text{ch}}(\Gamma)$ as a function of the average electronic density N calculated in the vicinity of the two PS boundaries defined by the chemical potentials μ_2 (red) and μ_3 (blue). The results are obtained at $T = 290$ K.

the corresponding channel. Thus, $\epsilon = 1$ indicates the absence of the fluctuations, and $\epsilon(\mathbf{Q}) = 0$ signals the formation of the ordered state with the ordering vector $\mathbf{q} = \mathbf{Q}$.

The largest dielectric function in the spin channel is found at the wave vector $\mathbf{q} = \mathbf{K} = \{4\pi/3, 0\}$, which corresponds to the 120° AFM type of spin fluctuations, in agreement with the finding of Ref. 18. However, by lowering the temperature from $T = 290$ K to 145 K the spin dielectric function changes from $\epsilon_{\omega=0}^{\text{sp}}(\mathbf{K}) = 0.97$ to $\epsilon_{\omega=0}^{\text{sp}}(\mathbf{K}) = 0.94$, which indicates that the magnetic fluctuations are relatively weak. Furthermore, a large extrapolated value of $\epsilon_{\omega=0}^{\text{sp}}(\mathbf{K}) = 0.91$ at $T = 0$ indicates that the system does not exhibit any tendency toward the formation of the spin ordered state, at least at the considered temperatures. Our calculations also do not reveal significant charge fluctuations. The largest dielectric function in the charge channel corresponds to the zero momentum $\mathbf{q} = \Gamma = \{0, 0\}$ and is very close to unity as well: $\epsilon_{\omega=0}^{\text{ch}}(\Gamma) = 0.96$ at $T = 290$ K and $\epsilon_{\omega=0}^{\text{ch}}(\Gamma) = 0.97$ at $T = 145$ K.

Doping the system does not alter the strength of the magnetic fluctuations, which are already weak in the considered material at half filling. However, we observe a significant change in the charge fluctuations upon doping. Figure 1 shows the evolution of the average electronic density N as a function of the chemical potential calculated at $T = 290$ K. Here, $\mu = 0$ corresponds to the undoped case of a half-filled Mott insulator. At $|\mu| \lesssim 0.8$ eV the chemical potential lies inside the gap and the system remains in the Mott insulating state with $N = 1$. At $|\mu| \gtrsim 0.8$ eV, taking into account only local correlations within DMFT results in a gradual increase of the electronic density with increasing chemical potential (blue curve). Importantly, no first-order phase transition is identified, which is consistent with other finite temperature single-site DMFT calculations of single-band models. Considering the non-local collective electronic fluctuations within the D-TRILEX approach drastically changes this picture (red curves). We find that in both electron ($N > 1$) and hole doped ($N < 1$) cases, the

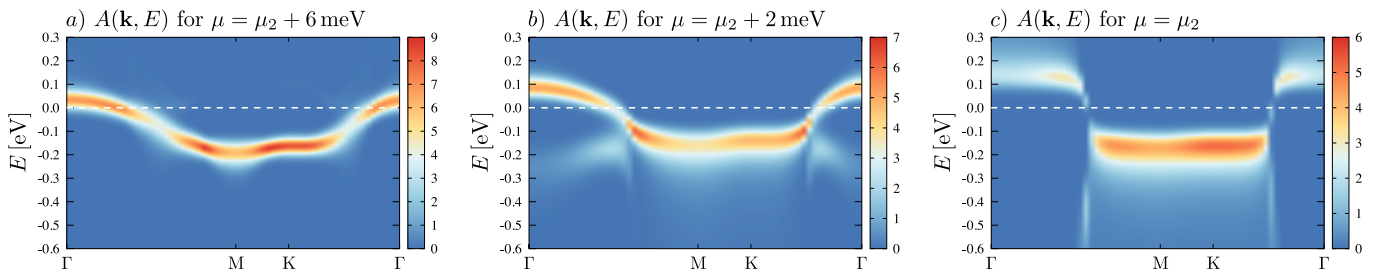


FIG. 3. Electronic spectral function. Evolution of the momentum-resolved electronic spectral function $A(\mathbf{k}, E)$ in the vicinity of the PS. The result is calculated at $T = 290$ K for $\mu = \mu_2 + 6$ meV (a), $\mu_2 + 2$ meV (b) and μ_2 (c), and plotted along the high-symmetry path in the BZ.

electronic compressibility $\kappa = \frac{1}{N^2} \frac{dN}{d\mu}$ diverges almost immediately when the chemical potential reaches the Hubbard bands. Importantly, this divergence occurs not only when approaching the Hubbard bands from half filling ($\mu_2 = -0.819$ eV and $\mu_3 = 0.871$ eV), but also from the unfilled ($\mu_1 = -1.068$ eV) and fully filled ($\mu_4 = 1.131$ eV) sides. The divergence of the compressibility indicates the appearance of the PS region, which is additionally confirmed by the divergence of the static dielectric function in the charge channel $\epsilon_{\omega=0}^{\text{ch}}(\mathbf{q})$ at the zero momentum $\mathbf{q} = \Gamma$, which occurs at the same values of the chemical potential (Figure 2). Extrapolating $\epsilon_{\omega=0}^{\text{ch}}(\Gamma)$ to zero shows that the PS occurs at $19.5 \pm 1.5\%$ of doping. At $\mu_1 < \mu < \mu_2$ and $\mu_3 < \mu < \mu_4$ the charge dielectric function remains divergent, defining the PS as regions of “forbidden” chemical potentials highlighted in red colour in Figure 2.

Importantly, the identified PS is formed differently than in other Mott insulators^{6–12}, where the PS appears between the two connected branches of the $N(\mu)$ curve. In our case, the $N(\mu)$ (red) curves in Figure 2 exhibit an upward trend in the vicinity of all four PS boundaries. This behaviour is linked to a strong asymmetry in the electronic density of states near the Fermi energy, which occurs when the chemical potential approaches the narrow Hubbard bands. This asymmetry causes a significant increase in the average electronic density due to strong charge fluctuations. As we approach the PS by increasing μ , which also increases N , we observe the expected rise in the $N(\mu)$ curve near μ_1 and μ_2 . Conversely, when approaching the PS by decreasing μ , the behaviour of the $N(\mu)$ curve near μ_2 and μ_4 becomes more complex. Further away from the PS, where both the charge fluctuations and the asymmetry in the density of states are small, the electronic density initially decreases with decreasing μ . However, in close proximity to the PS, the rapid increase in the strength of charge fluctuations and the asymmetry leads to a significant rise in N even as μ decreases, resulting in a region of negative compressibility. It is worth noting that since the charge dielectric function diverges within the PS regions, we cannot determine whether the two segments of the $N(\mu)$ curve on opposite sides of the PS regions are connected.

We also observe that the formation of the PS is related to a strong change in the electronic spectral function. Figure 3 shows the momentum-resolved spectral function $A(\mathbf{k}, E)$ plotted along the high-symmetry path in the Brillouin zone (BZ) that goes through the Γ , $M = (\pi, \pi/\sqrt{3})$ and K points. Far from the PS, at $\mu = \mu_2 + 6$ meV (a) the spectral function cor-

responds to the usual case of a hole-doped Mott insulator²⁷, with the quasi-particle peak at the Fermi energy ($E = 0$ depicted by the horizontal dashed white line) split from the lower Hubbard band ($E \simeq -0.2$ eV). Upon approaching the PS, the lower Hubbard band flattens, and at $\mu = \mu_2 + 2$ meV (b) the $A(\mathbf{k}, E)$ forms a pseudogap at $E = 0$ at the incommensurate momenta, which transforms to a gap at the PS boundary determined by μ_2 (c). We also observe the development of incoherent bands below the Fermi energy in close proximity to the PS. At $\mu = \mu_2 + 2$ meV (b) these bands appear rather close to $E = 0$, while at the PS boundary (c) they transform into almost straight lines localized at the incommensurate momenta where the gap is formed. The flattening of the Hubbard band and the emergence of incoherent bands below the Fermi energy stem from the increase in electronic density near the PS.

To understand the physical nature of the PS, let us examine the static charge susceptibility $X_{\omega=0}^{\text{ch}}(\mathbf{q})$ in the vicinity of μ_2 , as shown in the top row of Figure 4. We find that the divergence of the dielectric function is not visible in the susceptibility due to a very small value of the polarization operator at the Γ point. Instead, the largest value of the charge susceptibility corresponds to momenta at the edge of the BZ depicted by the black hexagon. Far from the PS, at $\mu = \mu_2 + 6$ meV (a) and $\mu = \mu_2 + 4$ meV (b), where the largest charge dielectric function is respectively equal to $\epsilon_{\omega=0}^{\text{ch}}(\Gamma) = 0.406$ and $\epsilon_{\omega=0}^{\text{ch}}(\Gamma) = 0.436$, the charge susceptibility is relatively small and its maximum is distributed over a rather large part of the BZ. As the PS is approached more closely (c), at $\mu = \mu_2 + 2$ meV ($\epsilon_{\omega=0}^{\text{ch}}(\Gamma) = 0.156$) the maximum of the susceptibility begins to localize at the edge of the BZ, but the value of the susceptibility still remains rather small. Finally, in close proximity to the PS, at $\mu = \mu_2 + 1$ meV, $\epsilon_{\omega=0}^{\text{ch}}(\Gamma) = 0.007$ (d) and μ_2 , $\epsilon_{\omega=0}^{\text{ch}}(\Gamma) = 0.002$ (f) the susceptibility drastically increases and displays a distinctive “bow-tie” shape with the maximum at the K point and the pinch-point at the M point. The appearance of the bow-tie structure in the spin susceptibility is one of the signatures of the formation of the spin ice state². By analogy with this state, we identify the observed bow-tie form of the charge susceptibility with a charge ice state. Remarkably, the bottom row of Figure 4 demonstrates that this state is formed at all chemical potentials that define the boundaries of the PS regions and only in close proximity to the PS ($\epsilon_{\omega=0}^{\text{ch}}(\Gamma) \lesssim 0.01$).

In the case of a spin ice, the bow-tie structure of the spin susceptibility in momentum space is a consequence of the

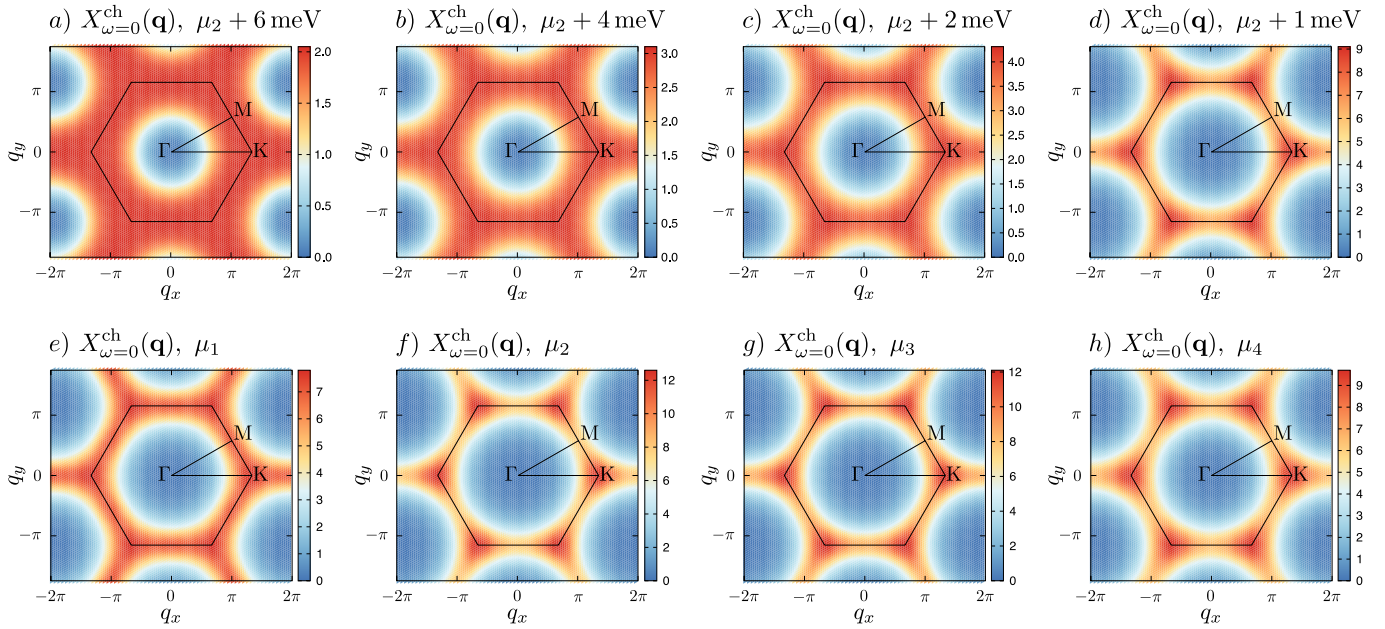


FIG. 4. Charge susceptibility. Top row: Evolution of the static charge susceptibility $X_{\omega=0}^{\text{ch}}(\mathbf{q})$ in the vicinity of the PS. The calculations are performed for $\mu = \mu_2 + 6$ meV (a), $\mu_2 + 4$ meV (b), $\mu_2 + 2$ meV (c) and $\mu_2 + 1$ meV (d). Bottom row: The static charge susceptibility obtained at different PS boundaries defined by the chemical potentials μ_1 (e), μ_2 (f), μ_3 (g) and μ_4 (h). All results are obtained at $T = 290$ K and shown in the momentum space (q_x, q_y) . The first BZ is depicted by the black hexagon. The high-symmetry points Γ , K and M are labeled explicitly.

dipolar correlations between the magnetic moments in real space, which decay as a power law $\sim 1/R^D$ with the distance R , where D is the dimension of the system^{38–40}. If the power law is reproduced exactly, the susceptibility at the M point shows a singularity. Deviation from the power law rounds this singularity, resulting in a rapidly decaying value of the susceptibility in the M – Γ direction, which corresponds to a finite correlation length of the spin ice state².

It has been shown in Ref. 41 that the correlated electronic system in the vicinity of the charge instability can be mapped onto an effective Ising model

$$H_{\text{eff}} = \frac{1}{2} \sum_{jj'} J_{jj'} \rho_j \rho_{j'}, \quad (2)$$

where $\rho_j = n_j - N$ is the difference of the electronic density on the site j from the average occupation of the system. The effective charge exchange interaction J , calculated following Ref. 41 in the vicinity of the PS (μ_2) as a function of the real space distance R , is shown in Figure 5. We find that further from the PS, at $\mu = \mu_2 + 6$ meV (green) the charge exchange interaction is highly frustrated. It has both, positive and negative values and the amplitude of $J(R)$ does not decay even at the distance of 10 lattice constants a . Reducing the chemical potential to $\mu = \mu_2 + 4$ meV (orange) suppresses the frustration and the long-range tail of the charge exchange interaction. Remarkably, only in a close proximity to the PS (blue and red), the long-range tail of the charge exchange interaction can be accurately fitted by the power-law dependence of the distance $J(R) \simeq 2/R^2$, as depicted by the black line. This result is consistent with the behaviour of the charge susceptibility that reveals the bow-tie structure only at the PS boundary

(Figure 4). In addition, the deviation of the first few nearest-neighbor interactions J from the power-law may explain the “rounded” singularity at the M point of the obtained charge susceptibility. We note that considering this power-law form for the dipolar coupling between the magnetic moments was found important for modeling the spin ice behaviour in Ising pyrochlore magnets^{42–46}. On the other hand, in some cases the power-law correlations between the magnetic moments in real space can also be realized by considering only the nearest-neighbour exchange interaction⁴⁴. Therefore, it is remarkable that the formation of the charge ice state is associated with the power-law form of both the correlations between the charge densities, reflected in the bow-tie form of the charge susceptibility, and the effective charge exchange interaction.

To conclude, in this work we have investigated collective electronic instabilities in the monolayer Nb_3Cl_8 . We have found that at half filling, the considered material lies deep in the Mott insulating phase and surprisingly does not reveal any tendency towards the formation of a charge or spin ordered state, contrary to some other Mott insulators with triangular lattice geometry^{13,14}. Upon doping, the system exhibits a region of PS, detected by a simultaneous divergence of the charge susceptibility (or dielectric function) at zero momentum Γ and the electronic compressibility. The critical doping required for the formation of the PS can be estimated through the extrapolation of the dielectric function to zero, resulting in an approximate value of 20% doping.

We observe that away from the PS, the charge susceptibility is rather small and weakly momentum-dependent. In turn, the effective exchange interaction between the charge densities is highly frustrated and long-ranged. However, in close

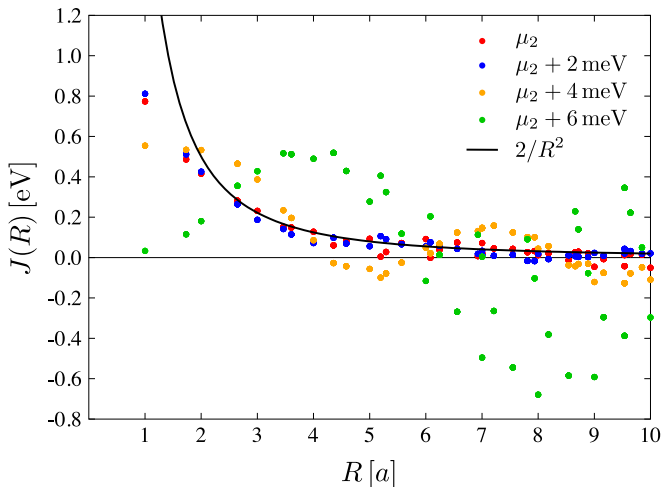


FIG. 5. Effective charge exchange interaction. The effective exchange interaction between the charge densities $J(R)$ calculated as a function of the real space distance R in units of the lattice constant a . The results are obtained at $T = 290$ K for $\mu = \mu_2 + 6$ meV (green), $\mu_2 + 4$ meV (orange), $\mu_2 + 2$ meV (blue) and μ_2 (red). The fit function $2/R^2$ is depicted by the solid black line.

proximity to the PS, the charge susceptibility dramatically increases and reveals a distinctive bow-tie pattern in momentum space, reminiscent of the magnetic susceptibility observed in the spin ice state. Simultaneously, the form of the charge exchange interaction undergoes a drastic change and acquires a power-law dependence in real space. These findings enable us to identify the PS as a charge ice state.

We find that the development of the charge ice state is accompanied by the formation of a gap and incoherent bands in the electronic spectral function. The appearance of the latter below the Fermi energy, along with the flattening of the Hubbard band, reflects the mechanism through which the electronic density increases upon approaching the PS. In turn, the gap in the electronic spectrum should not be seen as an indicator of an insulating phase, because the gap occurs at the incommensurate doping of the system. Instead, we relate it to the PS, which emerges as a consequence of the formation of the charge ice state. Indeed, unlike a conventional Ising model for spins, the introduced effective Ising model (2) has an additional constraint $\sum_i \rho_i = 0$ that is needed to fix the total occupation of the system. Unfortunately, we cannot access the real space structure of the charge ice state because we cannot perform symmetry-broken calculations inside the PS region. However, as in artificial spin ices^{47,48}, there one could expect the formation of “ferromagnetic” domains with higher and lower occupation than the averaged one, hence the PS.

Therefore, we find that the identified charge ice state, aside from the aforementioned constraint, is surprisingly similar to the spin ice state. It is also striking that the charge ice state has not been found in other Mott insulators with similar properties. For example, a system of Pb adatoms disposed periodically on a Si(111) surface also exhibits a triangular lattice geometry, features a strong and long-ranged Coulomb interaction, and lies deep in the Mott insulating state. Instead,

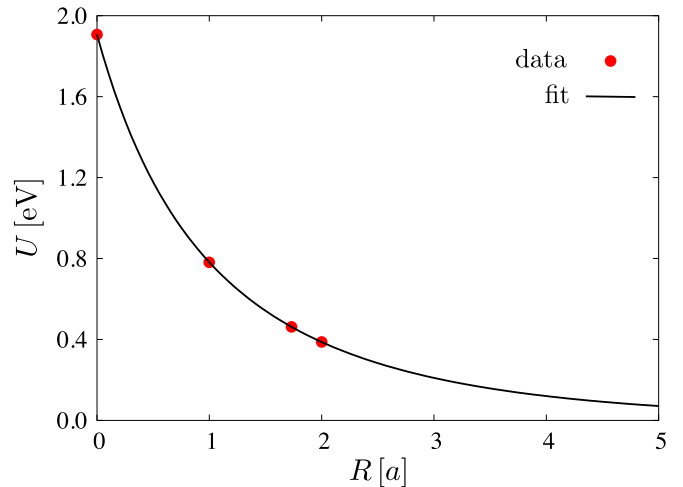


FIG. 6. Coulomb interaction. The red dots represent the values of the Coulomb interaction $U(R)$ up to the third nearest-neighbor distance in real space obtained in Ref. 18. The solid black line corresponds to the Yukawa-like form of the fit function introduced to account for the long-range tail of the Coulomb interaction.

upon doping, it reveals a charge density wave instability corresponding to the divergence of the charge susceptibility at a finite wave vector¹⁴. This emphasizes the necessity for a deeper understanding of the mechanism responsible for the formation of the charge ice state.

Methods

Model. The model (1) for the monolayer Nb_3Cl_8 is adopted from Ref. 18. The hopping amplitudes up to the third nearest-neighbor on a triangular lattice are: $t_1 = 22.6$ meV, $t_2 = 4.6$ meV and $t_3 = -4.0$ meV. The corresponding values of the Coulomb interaction U_j are depicted by the red dots in Figure 6. To reproduce the long-range tail of the Coulomb interaction we fit the real-space data $U(R)$ of Ref. 18 by the Yukawa-like potential $f(R) = C_1 \exp\{-C_2 R\}/(R + C_3)$, where $C_1 = 2.67$, $C_2 = 0.35$, and $C_3 = 1.40$. We find that Yukawa potential, which corresponds to a screened potential, better reproduces the short-range part of the Coulomb interaction than the conventional $\sim 1/R$ form.

Many-body calculations. The model Hamiltonian (1) is solved using the D-TRILEX approach^{24–26}. In D-TRILEX, local correlations are taken into account by solving the DMFT impurity problem²⁷, while non-local electronic effects are addressed by considering a leading subset of Feynman diagrams that describe electron scattering on collective charge and spin fluctuations^{28,29}. The impurity problem is solved using the w2DYNAMICS package⁴⁹. The diagrammatic part of the D-TRILEX method is calculated based on the numerical implementation described in Ref. 26. The local and momentum-resolved electronic spectral functions are obtained from the corresponding Matsubara Green’s functions via analytical continuation using the maximum entropy method implemented in the ANA_CONT package⁵⁰. The static charge susceptibilities are obtained using D-TRILEX, as described in Ref. 26.

Acknowledgments. E.A.S. thanks Alexander Kowalski and Giorgio Sangiovanni for the guidance in the $w2DYNAMICS$ calculations. E.A.S. also thanks Malte Rösner, Mikhail Katsnelson, Alexander Lichtenstein, Leon Balents, Maria

Chatzieftheriou and Luca de’ Medici for the fruitful discussions and valuable comments. The help of the CPHT computer support team is acknowledged as well.

- * evgeny.stepanov@polytechnique.edu
- ¹ N. F. Mott, *Metal-insulator transitions* (London: Taylor & Francis, 1974).
 - ² Leon Balents, “Spin liquids in frustrated magnets,” *Nature* **464**, 199–208 (2010).
 - ³ M. Grilli, R. Raimondi, C. Castellani, C. Di Castro, and G. Kotliar, “Superconductivity, phase separation, and charge-transfer instability in the $U=\infty$ limit of the three-band model of the CuO_2 planes,” *Phys. Rev. Lett.* **67**, 259–262 (1991).
 - ⁴ C. Castellani, C. Di Castro, and M. Grilli, “Singular Quasiparticle Scattering in the Proximity of Charge Instabilities,” *Phys. Rev. Lett.* **75**, 4650–4653 (1995).
 - ⁵ G. Kotliar, Sahana Murthy, and M. J. Rozenberg, “Compressibility Divergence and the Finite Temperature Mott Transition,” *Phys. Rev. Lett.* **89**, 046401 (2002).
 - ⁶ G. Sordi, K. Haule, and A.-M. S. Tremblay, “Finite Doping Signatures of the Mott Transition in the Two-Dimensional Hubbard Model,” *Phys. Rev. Lett.* **104**, 226402 (2010).
 - ⁷ G. Sordi, K. Haule, and A.-M. S. Tremblay, “Mott physics and first-order transition between two metals in the normal-state phase diagram of the two-dimensional Hubbard model,” *Phys. Rev. B* **84**, 075161 (2011).
 - ⁸ Jakob Steinbauer, Luca de’ Medici, and Silke Biermann, “Doping-driven metal-insulator transition in correlated electron systems with strong Hund’s exchange coupling,” *Phys. Rev. B* **100**, 085104 (2019).
 - ⁹ Maria Chatzieftheriou, Maja Berović, Pablo Villar Arribi, Massimo Capone, and Luca de’ Medici, “Enhancement of charge instabilities in Hund’s metals by breaking of rotational symmetry,” *Phys. Rev. B* **102**, 205127 (2020).
 - ¹⁰ L. Fratino, S. Bag, A. Camjayi, M. Civelli, and M. Rozenberg, “Doping-driven resistive collapse of the Mott insulator in a minimal model for VO_2 ,” *Phys. Rev. B* **105**, 125140 (2022).
 - ¹¹ Maria Chatzieftheriou, Alexander Kowalski, Maja Berović, Adriano Amaricci, Massimo Capone, Lorenzo De Leo, Giorgio Sangiovanni, and Luca de’ Medici, “Mott Quantum Critical Points at Finite Doping,” *Phys. Rev. Lett.* **130**, 066401 (2023).
 - ¹² P. O. Downey, O. Gingras, C. D. Hébert, M. Charlebois, and A. M. S. Tremblay, “Filling-induced Mott transition and pseudogap physics in the triangular lattice Hubbard model,” Preprint arXiv:2307.11190 (2023).
 - ¹³ C. Tresca, C. Brun, T. Bilgeri, G. Menard, V. Cherkov, R. Federicci, D. Longo, F. Debontridder, M. D’angelo, D. Roditchev, G. Profeta, M. Calandra, and T. Cren, “Chiral Spin Texture in the Charge-Density-Wave Phase of the Correlated Metallic $\text{Pb}/\text{Si}(111)$ Monolayer,” *Phys. Rev. Lett.* **120**, 196402 (2018).
 - ¹⁴ M. Vandelli, A. Galler, A. Rubio, A. I. Lichtenstein, S. Biermann, and E. A. Stepanov, “Doping-dependent charge- and spin-density wave orderings in a monolayer of Pb adatoms on $\text{Si}(111)$,” *npj Quantum Mater.* **9**, 19 (2024).
 - ¹⁵ Fangfei Ming, X Wu, C Chen, Kedong D Wang, Peizhi Mai, Thomas A Maier, J Strokoz, JWF Venderbos, Cesar González, Jose Ortega, *et al.*, “Evidence for chiral superconductivity on a silicon surface,” *Nat. Phys.* **19**, 500–506 (2023).
 - ¹⁶ Zhenyu Sun, Hui Zhou, Cuixiang Wang, Shiv Kumar, Daiyu Geng, Shaosheng Yue, Xin Han, Yuya Haraguchi, Kenya Shimada, Peng Cheng, Lan Chen, Youguo Shi, Kehui Wu, Sheng Meng, and Baojie Feng, “Observation of Topological Flat Bands in the Kagome Semiconductor Nb_3Cl_8 ,” *Nano Lett.* **22**, 4596–4602 (2022).
 - ¹⁷ Shunye Gao, Shuai Zhang, Cuixiang Wang, Shaohua Yan, Xin Han, Xuecong Ji, Wei Tao, Jingtong Liu, Tiantian Wang, Shuaikang Yuan, Gexing Qu, Ziyang Chen, Yongzhao Zhang, Jierui Huang, Mojun Pan, Shiyu Peng, Yong Hu, Hang Li, Yaobo Huang, Hui Zhou, Sheng Meng, Liu Yang, Zhiwei Wang, Yugui Yao, Zhiguo Chen, Ming Shi, Hong Ding, Huaixin Yang, Kun Jiang, Yunliang Li, Hechang Lei, Youguo Shi, Hongming Weng, and Tian Qian, “Discovery of a Single-Band Mott Insulator in a van der Waals Flat-Band Compound,” *Phys. Rev. X* **13**, 041049 (2023).
 - ¹⁸ Sergii Grytsiuk, Mikhail I Katsnelson, Erik GCP van Loon, and Malte Rösner, “ Nb_3Cl_8 : a prototypical layered Mott-Hubbard insulator,” *npj Quant. Mater.* **9**, 8 (2024).
 - ¹⁹ Yi Zhang, Yuhao Gu, Hongming Weng, Kun Jiang, and Jiangping Hu, “Mottness in two-dimensional van der Waals Nb_3X_8 monolayers ($X = \text{Cl}, \text{Br}, \text{and I}$),” *Phys. Rev. B* **107**, 035126 (2023).
 - ²⁰ Christopher M. Pasco, Ismail El Baggari, Elisabeth Bianco, Lena F. Kourkoutis, and Tyrel M. McQueen, “Tunable Magnetic Transition to a Singlet Ground State in a 2D van der Waals Layered Trimerized Kagomé Magnet,” *ACS Nano* **13**, 9457–9463 (2019).
 - ²¹ John P. Sheckelton, Kemp W. Plumb, Benjamin A. Trump, Collin L. Broholm, and Tyrel M. McQueen, “Rearrangement of van der Waals stacking and formation of a singlet state at $T = 90$ K in a cluster magnet,” *Inorg. Chem. Front.* **4**, 481–490 (2017).
 - ²² Yuya Haraguchi, Chishiro Michioka, Manabu Ishikawa, Yoshiaki Nakano, Hideki Yamochi, Hiroaki Ueda, and Kazuyoshi Yoshimura, “Magnetic–Nonmagnetic Phase Transition with Inter-layer Charge Disproportionation of Nb_3 Trimers in the Cluster Compound Nb_3Cl_8 ,” *Inorg. Chem.* **56**, 3483–3488 (2017).
 - ²³ Jiho Yoon, Edouard Lesne, Kornelia Sklarek, John Sheckelton, Chris Pasco, Stuart S P Parkin, Tyrel M McQueen, and Mazhar N Ali, “Anomalous thickness-dependent electrical conductivity in van der Waals layered transition metal halide, Nb_3Cl_8 ,” *J. Phys.: Condens. Matter* **32**, 304004 (2020).
 - ²⁴ E. A. Stepanov, V. Harkov, and A. I. Lichtenstein, “Consistent partial bosonization of the extended Hubbard model,” *Phys. Rev. B* **100**, 205115 (2019).
 - ²⁵ V. Harkov, M. Vandelli, S. Brener, A. I. Lichtenstein, and E. A. Stepanov, “Impact of partially bosonized collective fluctuations on electronic degrees of freedom,” *Phys. Rev. B* **103**, 245123 (2021).
 - ²⁶ Matteo Vandelli, Josef Kaufmann, Mohammed El-Nabulsi, Viktor Harkov, Alexander I. Lichtenstein, and Evgeny A. Stepanov, “Multi-band D-TRILEX approach to materials with strong electronic correlations,” *SciPost Phys.* **13**, 036 (2022).
 - ²⁷ Antoine Georges, Gabriel Kotliar, Werner Krauth, and Marcelo J. Rozenberg, “Dynamical mean-field theory of strongly correlated fermion systems and the limit of infinite dimensions,” *Rev. Mod.*

- Phys.* **68**, 13–125 (1996).
- ²⁸ G. Rohringer, H. Hafermann, A. Toschi, A. A. Katanin, A. E. Antipov, M. I. Katsnelson, A. I. Lichtenstein, A. N. Rubtsov, and K. Held, “Diagrammatic routes to nonlocal correlations beyond dynamical mean field theory,” *Rev. Mod. Phys.* **90**, 025003 (2018).
 - ²⁹ Ya. S. Lyakhova, G. V. Astretsov, and A. N. Rubtsov, “The mean-field concept and post-DMFT methods in the contemporary theory of correlated systems,” *Phys. Usp.* **66**, 775–793 (2023).
 - ³⁰ Evgeny A. Stepanov, Yusuke Nomura, Alexander I. Lichtenstein, and Silke Biermann, “Orbital Isotropy of Magnetic Fluctuations in Correlated Electron Materials Induced by Hund’s Exchange Coupling,” *Phys. Rev. Lett.* **127**, 207205 (2021).
 - ³¹ Evgeny A. Stepanov, “Eliminating Orbital Selectivity from the Metal-Insulator Transition by Strong Magnetic Fluctuations,” *Phys. Rev. Lett.* **129**, 096404 (2022).
 - ³² M. Vandelli, J. Kaufmann, V. Harkov, A. I. Lichtenstein, K. Held, and E. A. Stepanov, “Extended regime of metastable metallic and insulating phases in a two-orbital electronic system,” *Phys. Rev. Res.* **5**, L022016 (2023).
 - ³³ Maria Chatzieftheriou, Silke Biermann, and Evgeny A. Stepanov, “Local and nonlocal electronic correlations at the metal-insulator transition in the Hubbard model in two dimensions,” Preprint arXiv:2312.03123 (2023).
 - ³⁴ Evgeny A. Stepanov and Silke Biermann, “Can Orbital-Selective Néel Transitions Survive Strong Nonlocal Electronic Correlations?” *Phys. Rev. Lett.* **132**, 226501 (2024).
 - ³⁵ Evgeny A. Stepanov, Maria Chatzieftheriou, Niklas Wagner, and Giorgio Sangiovanni, “Interconnected Renormalization of Hubbard Bands and Green’s Function Zeros in Mott Insulators Induced by Strong Magnetic Fluctuations,” Preprint arXiv:2402.02814 (2024).
 - ³⁶ E. A. Stepanov, V. Harkov, M. Rösner, A. I. Lichtenstein, M. I. Katsnelson, and A. N. Rudenko, “Coexisting charge density wave and ferromagnetic instabilities in monolayer InSe,” *npj Comput. Mater.* **8**, 118 (2022).
 - ³⁷ Evgeny A. Stepanov, Matteo Vandelli, Alexander I. Lichtenstein, and Frank Lechermann, “Charge Density Wave Ordering in NdNiO₂: Effects of Multiorbital Nonlocal Correlations,” *npj Comput. Mater.* **10**, 108 (2024).
 - ³⁸ S. V. Isakov, K. Gregor, R. Moessner, and S. L. Sondhi, “Dipolar Spin Correlations in Classical Pyrochlore Magnets,” *Phys. Rev. Lett.* **93**, 167204 (2004).
 - ³⁹ C. L. Henley, “Power-law spin correlations in pyrochlore antiferromagnets,” *Phys. Rev. B* **71**, 014424 (2005).
 - ⁴⁰ T. Fennell, P. P. Deen, A. R. Wildes, K. Schmalzl, D. Prabhakaran, A. T. Boothroyd, R. J. Aldus, D. F. McMorrow, and S. T. Bramwell, “Magnetic Coulomb Phase in the Spin Ice Ho₂Ti₂O₇,” *Science* **326**, 415–417 (2009).
 - ⁴¹ E. A. Stepanov, A. Huber, A. I. Lichtenstein, and M. I. Katsnelson, “Effective Ising model for correlated systems with charge ordering,” *Phys. Rev. B* **99**, 115124 (2019).
 - ⁴² R. Siddharthan, B. S. Shastry, A. P. Ramirez, A. Hayashi, R. J. Cava, and S. Rosenkranz, “Ising Pyrochlore Magnets: Low-Temperature Properties, “Ice Rules,” and Beyond,” *Phys. Rev. Lett.* **83**, 1854–1857 (1999).
 - ⁴³ Byron C. den Hertog and Michel J. P. Gingras, “Dipolar Interactions and Origin of Spin Ice in Ising Pyrochlore Magnets,” *Phys. Rev. Lett.* **84**, 3430–3433 (2000).
 - ⁴⁴ Steven T. Bramwell and Michel J. P. Gingras, “Spin Ice State in Frustrated Magnetic Pyrochlore Materials,” *Science* **294**, 1495–1501 (2001).
 - ⁴⁵ Taras Yavors’kii, Tom Fennell, Michel J. P. Gingras, and Steven T. Bramwell, “Dy₂Ti₂O₇ Spin Ice: A Test Case for Emergent Clusters in a Frustrated Magnet,” *Phys. Rev. Lett.* **101**, 037204 (2008).
 - ⁴⁶ Steven T. Bramwell and Mark J. Harris, “The history of spin ice,” *J. Phys.: Condens. Matter* **32**, 374010 (2020).
 - ⁴⁷ R. F. Wang, C. Nisoli, R. S. Freitas, J. Li, W. McConville, B. J. Cooley, M. S. Lund, N. Samarth, C. Leighton, V. H. Crespi, and P. Schiffer, “Artificial ‘spin ice’ in a geometrically frustrated lattice of nanoscale ferromagnetic islands,” *Nature* **439**, 303–306 (2006).
 - ⁴⁸ Cristiano Nisoli, Roderich Moessner, and Peter Schiffer, “Colloquium: Artificial spin ice: Designing and imaging magnetic frustration,” *Rev. Mod. Phys.* **85**, 1473–1490 (2013).
 - ⁴⁹ Markus Wallerberger, Andreas Hausoel, Patrik Gunacker, Alexander Kowalski, Nicolaus Parragh, Florian Goth, Karsten Held, and Giorgio Sangiovanni, “w2dynamics: Local one- and two-particle quantities from dynamical mean field theory,” *Computer Physics Communications* **235**, 388–399 (2019).
 - ⁵⁰ Josef Kaufmann and Karsten Held, “ana_cont: Python package for analytic continuation,” ArXiv e-prints (2021), arXiv:2105.11211.